Article

Degradation of Organic Dyes by the UCNP/h-BN/TiO$_2$ Ternary Photocatalyst

Weijun Xie, Yue Zhang, Lei Xu, Dan Xie, Li Jiang, Yanmao Dong, and Yan Yuan*

Cite This: *ACS Omega* 2023, 8, 48662−48672

Read Online

ACCESS | Metrics & More | Article Recommendations | Supporting Information

ABSTRACT: In this study, upconversion nanoparticles (UCNPs) with a flower-like morphology were prepared using a urea coprecipitation method. A ternary photocatalyst was first prepared using a solvothermal method involving the use of titanium oxide (TiO$_2$), hexagonal boron nitride (h-BN), and UCNPs (Y$_2$O$_3$, Yb^{3+}, and Tm^{3+}) as raw materials. The surface morphology, crystal structure, and functional groups of these materials were then characterized and analyzed through scanning electron microscopy, transmission electron microscopy, X-ray diffraction analysis, Fourier transform infrared spectroscopy, X-ray photoelectron spectroscopy, ultraviolet−visible spectrophotometry, and other techniques. Photocatalytic experiments were also conducted to investigate the effects of different catalyst types, raw material doping ratios, pH values, and catalyst quantities on the photocatalytic degradation of rhodamine B (RhB). The results indicated that doping with h-BN and UCNPs reduced the band gap width of RhB, increased its light absorption rate, and decreased the recombination rate of its photogenerated electrons and holes so that the photocatalytic degradation effect reached 100% within 2 h. After five experimental cycles, the 30% UC-BN-Ti photocatalyst remained highly durable and stable. To investigate the effects of different trapping agents on the degradation of RhB, benzoquinone, isopropanol, and ethylenediaminetetraacetic acid disodium salt were used as free-radical-capturing agents. The results indicated that •O$^{2−}$ was the primary active species in the degradation process. Finally, the pathway and mechanism of the degradation of RhB through ternary composite photocatalysis were identified.
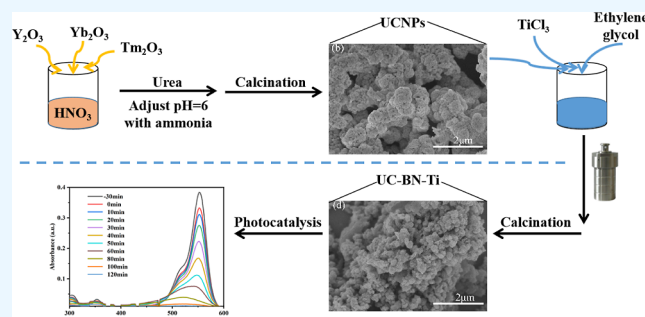
1. INTRODUCTION

The textile industry has rapidly expanded in China.[1] Currently, the annual production of dyes in China has reached 9 billion tons, which represents 70% of the global dye output.[2,3] However, the production and use of dyes result in the generation of a large quantity of dye-contaminated wastewater, which requires treatment.[4,5] Dye wastewater is characterized by complex components and a dark color, and its discharge into water bodies reduces the water's transparency and negatively affects the growth of aquatic organisms. Dye wastewater is also carcinogenic, teratogenic, mutagenic, and extremely hazardous to the health of humans and other organisms.[6]

Dye wastewater contains azo groups, heterocycles, and benzene rings that are difficult to degrade. The currently used methods for treating dye wastewater include physical, biological, chemical, and photocatalytic methods. Physical methods, including physical adsorption and membrane separation, are simple but result in the incomplete treatment of dye wastewater.[5,7,8] Biological methods involve the separation or degradation of organic dyes into inorganic products and intermediates through the adsorption, flocculation, and degradation of bacteria.[9] Chemical methods,

including electrochemical methods and advanced oxidation methods, involve reactions induced between reactive substances and dyes by light, electricity, and magnetism, which result in the oxidation and decomposition of dyes into nontoxic or weakly toxic small molecules.[10,11]

Photocatalysis refers to the degradation of toxic macromolecular pollutants into nontoxic or weakly toxic small molecular substances under ultraviolet (UV) light.[1] Titanium oxide (TiO$_2$) is a semiconductor photocatalyst that is widely used because of its biocompatibility, stable chemical properties, low cost, and favorable photocatalytic activity.[12] However, the application of TiO$_2$ is limited by its large band gap, high photogenerated electron−hole recombination rate, and low utilization of natural light.
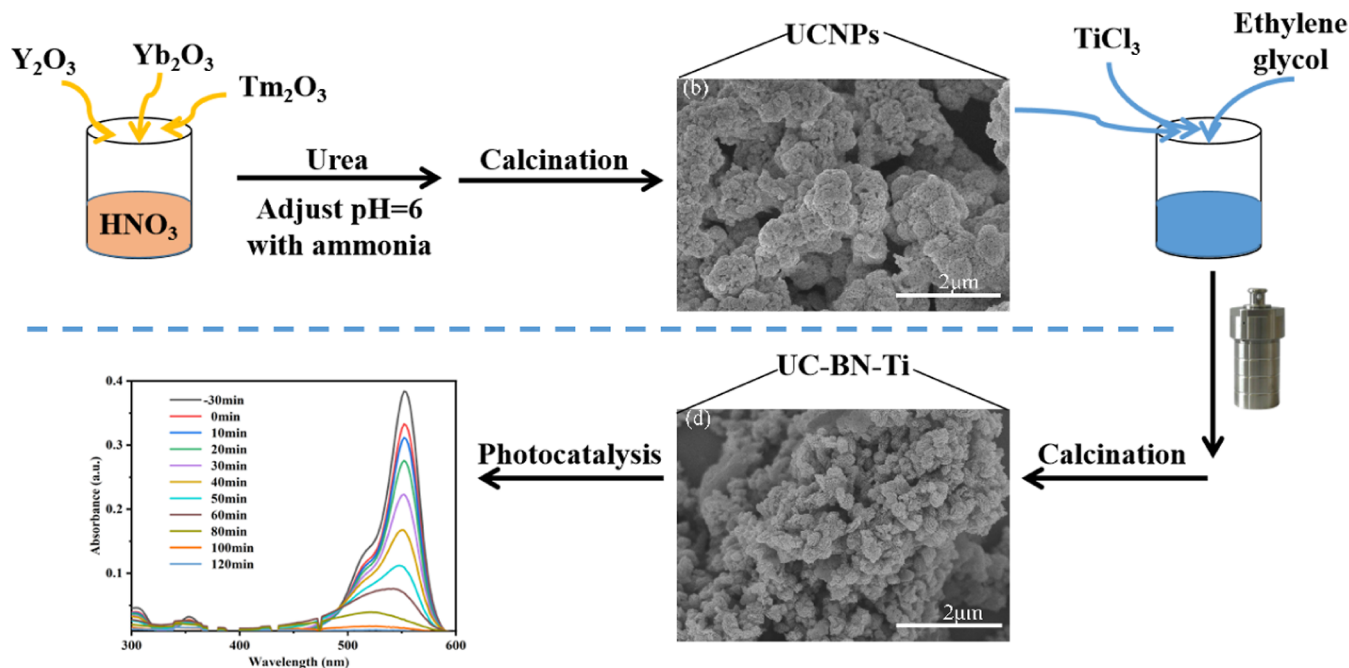
Numerous studies have indicated that combining hexagonal boron nitride (h-BN) with semiconductors such as h-BN/
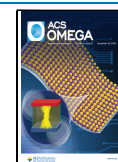
Scheme 1. Preparation Route of the UCNP/h-BN/TiO$_2$ Ternary Photocatalyst

BiMoO$_6$,[13] h-BN/CdS,[14] h-BN/Ag$_3$PO$_4$,[15] h-BN/Sb$_2$WO$_6$,[16] h-BN/a-SnWO$_4$,[17] h-BN/graphene,[18] h-BN/g-C$_3$N$_4$,[19] h-BN/WS$_2$,[20] and h-BN/MoTe$_2$[21] may result in an improved photocatalytic effect. Song[14] synthesized h-BN/CdS composites by using a one-step hydrothermal method. h-BN and CdS form a heterostructure that can improve the efficiency of charge transfer and strongly inhibit electron−hole recombination. In addition, h-BN/CdS composites can strongly inhibit the agglomeration of CdS nanospheres. Regarded as an excellent carrier of photocatalysts, h-BN is an environmentally friendly two-dimensional, graphene-like structure with excellent physical and chemical stability and high biocompatibility.[22−24] Its two-dimensional planar structure makes it an effective electron acceptor and allows it to reduce the electron−hole recombination rate of TiO$_2$ excited by UV light.[25]

Upconversion nanoparticles (UCNPs) refer to rare-earth-ion-doped materials that convert low-energy, near-infrared (NIR) light into high-energy, UV light, or visible light.[26] UCNPs are primarily composed of a matrix, a sensitizer, and an activator. According to previous studies on BiOCl/UCNP,[27] Ag/Bi$_2$O$_3$/UCNP,[28] Bi$_2$WO$_6$/UCNP,[29] and TiO$_2$/UCNP.[30,31] UCNPs can increase the light absorption of materials. Zhang[32] prepared a core−shell nanohybrid material for visible/NIR photocatalysis. They used a hydrothermal method to assemble a bismuth ferrite (BFO) shell around a core consisting of NaGdF$_4$/Er^{3+}/Yb^{3+}. Although the BFO and UCNPs alone did not exhibit any photocatalytic activity under NIR irradiation, the UCNP@BFO nanostructure photodegraded pollutants under NIR light because of the combination of the upconversion mechanisms and non-radiative energy transfer between the BFO and UCNPs.

In the present study, to investigate the photocatalytic degradation effects of UCNPs on dyes under UV−visible (UV−Vis) light, we prepared a ternary composite photocatalyst by using a solvothermal method involving the use of TiO$_2$, h-BN, and UCNPs (Y$_2$O$_3$, Yb^{3+}, and Tm^{3+}) as raw materials. After we identified the primary active species, we

discovered that the photocatalytic efficiency of the prepared UC-BN-Ti composites considerably improved, which we attributed to the efficient separation of the carriers generated by photons and the enhancement of the light absorption intensity.

2. MATERIALS AND METHODS

2.1. Materials. TiCl$_3$, Na$_2$SO$_4$, and HNO$_3$ were purchased from Shanghai Lingfeng Chemical Reagent (Shanghai, China). Ethylene glycol, sodium chloride, p-benzoquinone (p-BQ), ethylenediaminetetraacetic acid disodium salt (EDTA-2Na), and anhydrous sodium carbonate were purchased from Sinopharm Chemical Reagent (Shanghai, China). Ethanol, isopropanol (IPA), and NH$_3$·H$_2$O were purchased from Jiangsu Qiangsheng Functional Chemical (Suzhou, China). Urea was purchased from Wuxi Jingke Chemical (Jiangsu, China). Finally, h-BN (purity ≥ 99.9%), Yb$_2$O$_3$, Y$_2$O$_3$, Tm$_2$O$_3$, rhodamine B (RhB), methylene blue (MB), and azorubine (SXH) were purchased from Shanghai Aladdin Biochemical Technology (Shanghai, China).

2.2. Preparation of UCNPs. UCNPs were prepared by urea coprecipitation.[33,34] Y$_2$O$_3$, Yb$_2$O$_3$, and Tm$_2$O$_3$ were added into 20 mL of HNO$_3$ with a volume fraction of 50% and heated to dissolve. Then, a certain amount of urea was added to the solution and 300 mL of deionized water was added after urea was dissolved. The pH of the mixture was adjusted to about 6 with NH$_3$·H$_2$O, and then the mixture was reacted at 85 °C for 4 h. After standing for 3 h, the precipitate was centrifuged and washed once with deionized water and once with ethanol, respectively. The precipitate was dried for 12 h in an oven at 70 °C and ground into a powder. At last, the powder was calcined for 3 h in a muffle furnace at 800 °C.

2.3. Preparation of Photocatalysts. Preparation of h-BN/TiO$_2$: 60 mL of ethylene glycol, 2 mL of TiCl$_3$, 2 mL of deionized water, and a certain amount of h-BN were added into a 100 mL Teflon-lined stainless-steel autoclave, and the reactants were reacted at 150 °C for 12 h. After the product
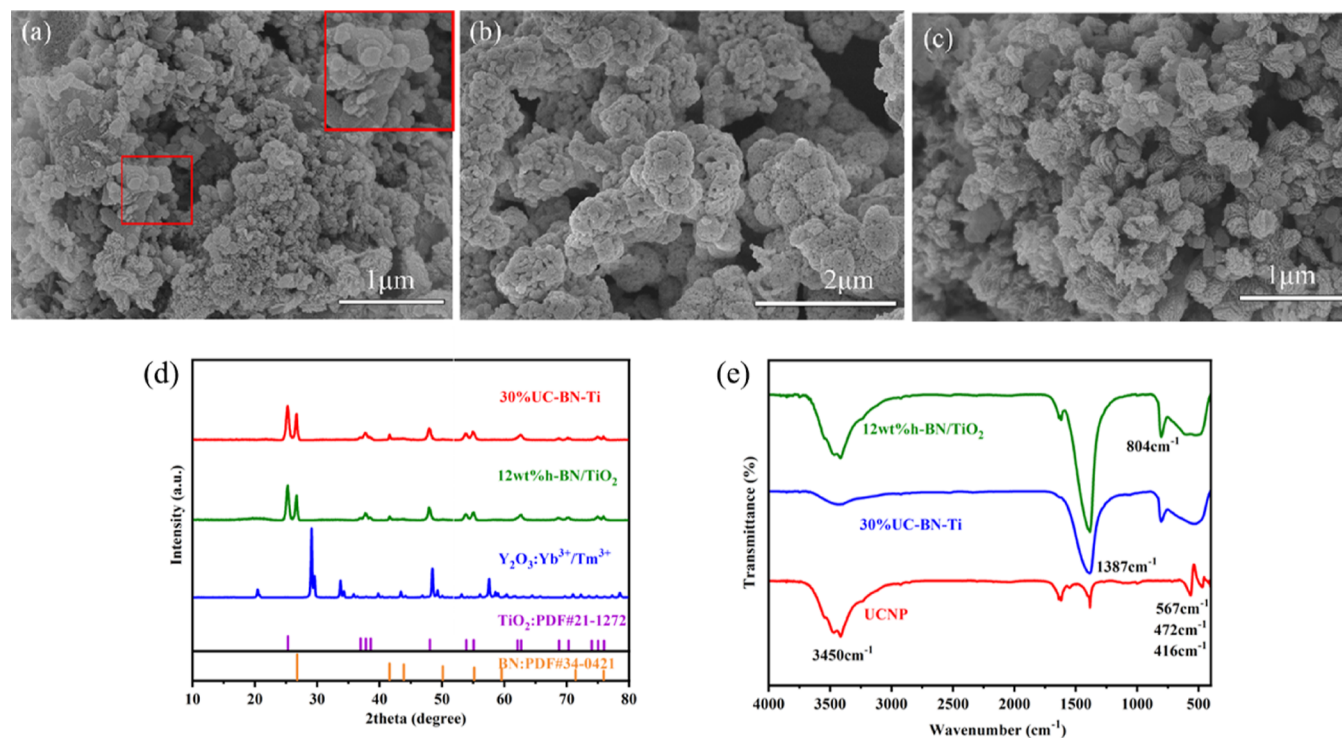
Figure 1. SEM results of (a) 12 wt % h-BN/TiO$_2$, (b) UCNPs, (c) 30 wt % UC-BN-Ti, (d) XRD, and (e) FT-IR results of 30% UC-BN-Ti, 12 wt % h-BN/TiO$_2$, and UCNPs.

was cooled down, it was centrifuged and washed twice with ethanol. Then, the product was dried at 70 °C overnight to obtain a white powder. After grinding, the powder was calcined at 500 °C for 2 h. The obtained sample was named X wt % h-BN/TiO$_2$, where X refers to the mass fraction of h-BN in the synthetic process.[35,36]

Preparation of UC-TiO$_2$: 60 mL of ethylene glycol, 2 mL of TiCl$_3$, 2 mL of deionized water, and a certain amount of UCNPs were added into a 100 mL Teflon-lined stainless-steel autoclave. Other operations were the same as described in the preparation of h-BN/TiO$_2$.

Preparation of UCNP/h-BN/TiO$_2$ (UC-BN-Ti for short): 60 mL of ethylene glycol, 2 mL of TiCl$_3$, 2 mL of deionized water, and a certain amount of h-BN and UCNPs were added into a 100 mL Teflon-lined stainless-steel autoclave. Other operations were the same as described in the preparation of h-BN/TiO$_2$. The product obtained was named Y % UC-BN-Ti, and Y refers to the mass fraction of UCNP/(UCNP + h-BN). The preparation route is shown in Scheme 1.

2.4. Characterization. Scanning electron microscopy (SEM; Hitachi Regulus 8100) and transmission electron microscopy (TEM; FEI Talos F200S) were used to examine the microstructural characteristics of the prepared samples. X-ray diffraction (XRD) analysis (Rigaku D/Max-2200PC, Japan) was conducted to characterize the crystal structure of the samples. Fourier transform infrared (FT-IR) spectra of the samples were recorded using a Bruker Vertex 70 FT-IR spectrophotometer by using the KBr compression technique. X-ray photoelectron spectroscopy (XPS; Thermo Scientific K-Alpha) was used to analyze the surfaces of the samples. The porous characteristics of the samples were investigated using nitrogen adsorption−desorption isotherms recorded at −196 °C by using a Micromeritics ASAP 2460 surface area and porosity analyzer. The surface area was then calculated from the nitrogen adsorption isotherms at a relative pressure of 0.05−0.025 by using the Brunauer−Emmett−Teller (BET) method. A Shimadzu UV-3600i Plus UV/visible/NIR diffuse reflectometer (Japan) was used to analyze the band-gap widths of the samples. A steady-state/instantaneous fluorescence spectrometer (model FLS1000; Edinburgh, United Kingdom) was used to analyze the upconversion luminescence (UCL) of the samples. The photocurrent responses of the samples were analyzed using the $i−t$ test of electrochemical workstations, and the electron−hole recombination rates of different samples were compared. A total organic carbon (TOC) analyzer (Shimadzu TOC-L CPN, Japan) was used to test the organic carbon and total inorganic carbon content in water samples before and after the photocatalytic reaction. A high-pressure liquid chromatography−mass spectrometry system (Ultimate 3000 UHPLC-Q Exactive) equipped with a UV−vis diode array detector using an Eclipse Plus C18 column (100 mm × 4.6 mm, 3.5 μm) was used to test for possible degradation products of RhB after 2 h of photocatalytic reaction. The HPLC separation was carried out using mixed eluents (CH$_3$OH/H$_2$O = 70:30 by volume) at a flow rate of 0.6 mL·min^{-1}.

2.5. Photoelectrochemical Measurement. Indium tin oxide glass was used as the test electrode, Ag/AgCl was used as the reference electrode, and platinum was used as the counter electrode. A CHI660D electrochemical workstation was used to observe the photocurrent response of the samples. The initial voltage was 0 V, and the photocurrent and irradiation time curves were recorded for 40 s under dark conditions and 40 s under light conditions, respectively.[37] The light source used in the procedure was a 300 W Xe lamp with a 400 nm cutoff filter and an optical density of 100 mW·cm^{-2}.

2.6. Photocatalytic Experiment. The photocatalytic activity of the UC-BN-Ti ternary composite photocatalyst
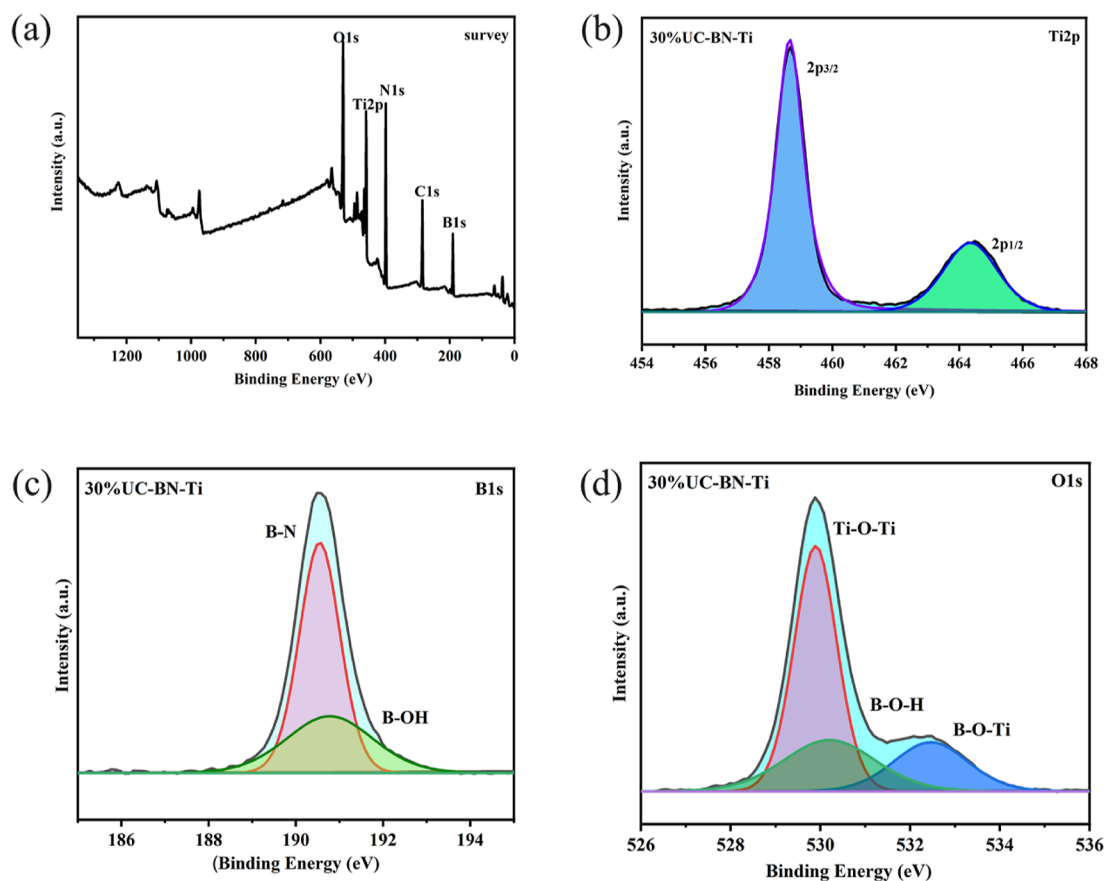
Figure 2. (a) Survey, (b) Ti 2p, (c) B 1s, and (d) O 1s XPS spectra of 30% UC-BN-Ti.

was determined through the UV−vis light degradation of RhB in an aqueous solution. In this test, a Xe lamp with an intensity of 100 mW·cm^{-2} was used as a UV−vis light source (300 W) at room temperature. A light intensity meter was used to measure the radiation flux per unit area in the reactor in the visible-light range, and the air input was set as 40 mL·min^{-1}. Subsequently, 60 mg of the powder was dispersed into 600 mL of a RhB solution (0.02 mmol·L^{-1}), and the suspension was stirred for 30 min in the dark to achieve adsorption−desorption equilibrium. Next, 10 mL of the solution was extracted from the suspension every 20 min, filtered using a 0.22 μm syringe, and analyzed using a UV−vis spectrophotometer to determine the residual concentration of RhB at 552 nm. The prepared h-BN/TiO$_2$ and UC-TiO$_2$ photocatalysts were used for comparison. The removal efficiency of RhB was calculated using eq 1, and the removal kinetics were calculated using eq 2.[38]

$$Y = \frac{C}{C_0} \tag{1}$$

$$\mathrm{Ln}\left(\frac{C_0}{C}\right) = kt \tag{2}$$

where C_0 is the initial concentration of RhB (0.02 mmol·L^{-1}), C is the concentration of RhB within the required time interval, k is the removal rate constant, and t is the time.

2.7. Recycling of Different Photocatalysts. Because h-BN/TiO$_2$ and UC-BN-Ti are fine powders, recovering these catalysts through static precipitation in water is difficult; therefore, centrifugation was performed for catalyst recovery.

To conduct an adsorption/photocatalytic synergistic experiment, 60 mg of UC-BN-Ti was added to 600 mL of a RhB solution with a concentration of 0.02 mmol·L^{-1}. The same concentration of the RhB solution was then added between each cycle without cleaning or drying. The aforementioned process was also used for the BN/TiO$_2$ catalyst.

3. RESULTS AND DISCUSSION

3.1. Characterization of Photocatalysts. Figure 1a depicts an SEM image of the h-BN/TiO$_2$ binary photocatalyst, Figure 1b depicts an SEM image of UCNPs (Y$_2$O$_3$: Yb^{3+}/Tm^{3+}), and Figure 1c depicts an SEM image of the UC-BN-Ti ternary photocatalyst. As shown in Figure 1a, h-BN had a lamellar structure, and TiO$_2$ had a short rod-like structure. As displayed in Figure 1b, the UCNPs had a uniform and stable flower-like structure. As depicted in Figure 1c, the ternary composites had a cluster-like structure. XRD was used to analyze the crystal structure and phase purity of the samples. Figure 1d depicts the XRD patterns of UCNPs, 12 wt % h-BN/TiO$_2$, and 30% UC-BN-Ti. The 12 wt % h-BN/TiO$_2$ and 30% UC-BN-Ti samples exhibited characteristic peaks at 25.24 and 26.7°, which corresponded to the (101) crystal plane of anatase-phase TiO$_2$ and the (002) crystal plane of h-BN, respectively.[39] However, no characteristic peak was observed for UCNPs in the ternary composite photocatalyst, presumably because the doping quantity of UCNPs in the ternary composite photocatalyst was small and the characteristic peaks were covered by those of other components. Figure 1e depicts the characteristic peaks for the O−H group at 3450 cm^{-1} and TiO$_2$ at 500−750 cm^{-1}. The characteristic peak at
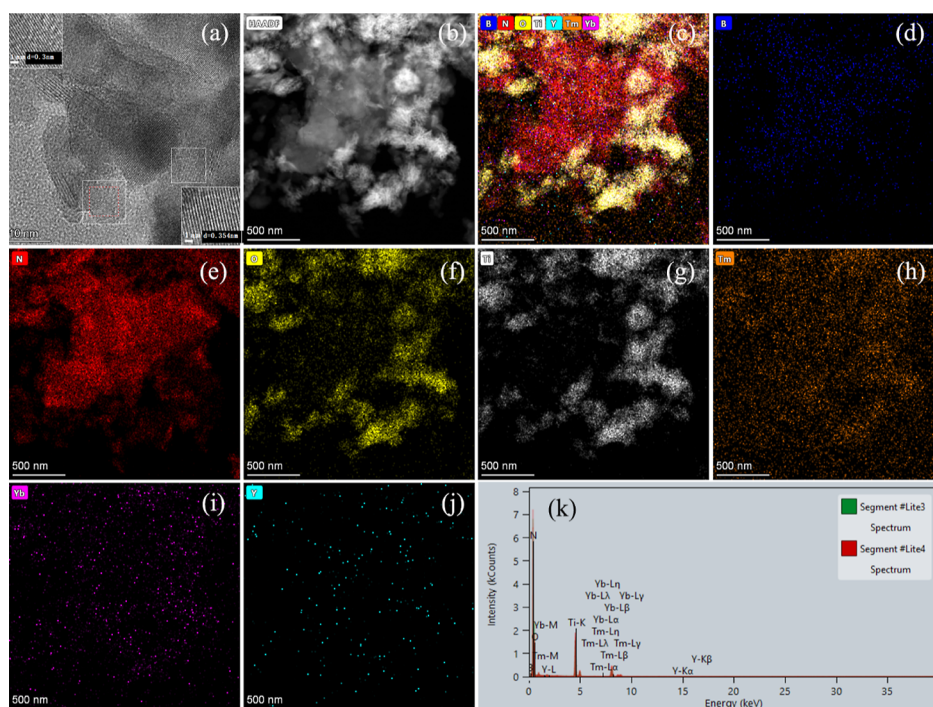
Figure 3. (a) TEM image of the UC-BN-Ti composite, (b) high-angle annular dark-field image of the UC-BN-Ti composite, (c−j) elemental compositions of the UC-BN-Ti composite, and (k) results of energy-dispersive X-ray analysis for the UC-BN-Ti composite.
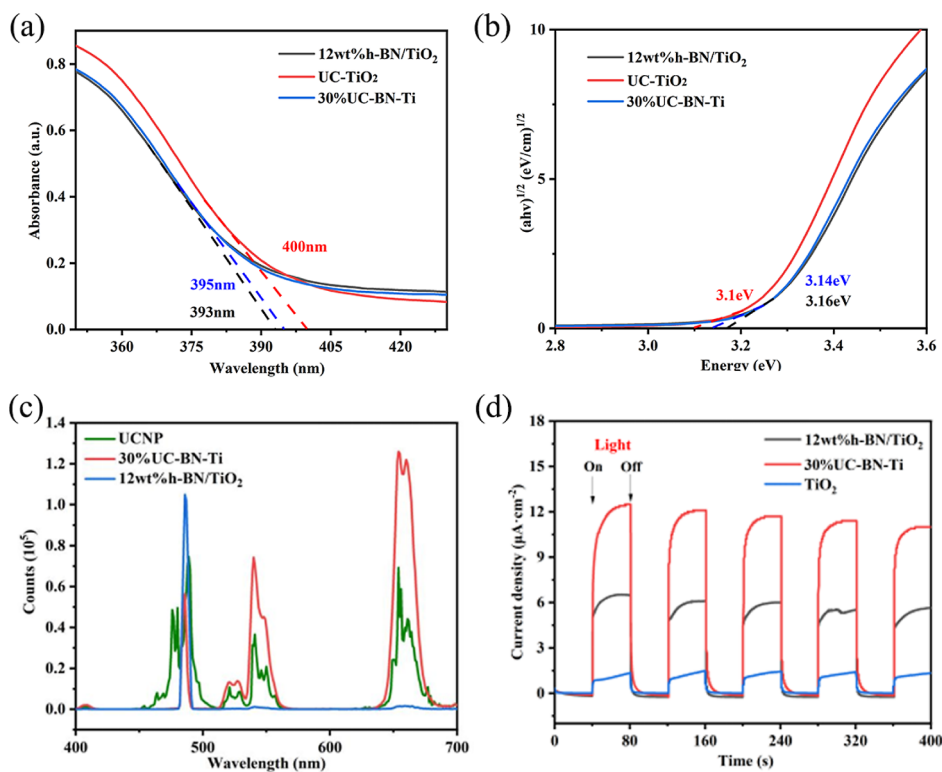

Figure 4. UV−vis diffuse reflection spectra: (a) Kubelka−Munk plots and (b) photocurrent−time curves of 12 wt % h-BN/TiO$_2$, UC-TiO$_2$, and 30% UC-BN-Ti, (c) UCL spectra of UCNPs, 30% UC-BN-Ti, and 12 wt % h-BN/TiO$_2$, (d) Photocurrent responses of 30% UC-BN-Ti and 12 wt % h-BN/TiO$_2$.

804 cm^{-1} corresponded to the bending vibration peak of the B−N−B bond, and the characteristic peak at 1387 cm^{-1} corresponded to the stretching vibration peak of the B−N bond. Both peaks were observed in the FT-IR curves of 12 wt % h-BN/TiO$_2$ and 30% UC-BN-Ti. This result indicated the

presence of h-BN and TiO$_2$ in both photocatalysts. The UCNP curves had peaks at 416 and 472 cm^{-1}. The peak at 567 cm^{-1} corresponded to the stretching vibration peak of the Y−O bond, and this peak may have been covered by other peaks in the curves of 30% UC-BN-Ti.
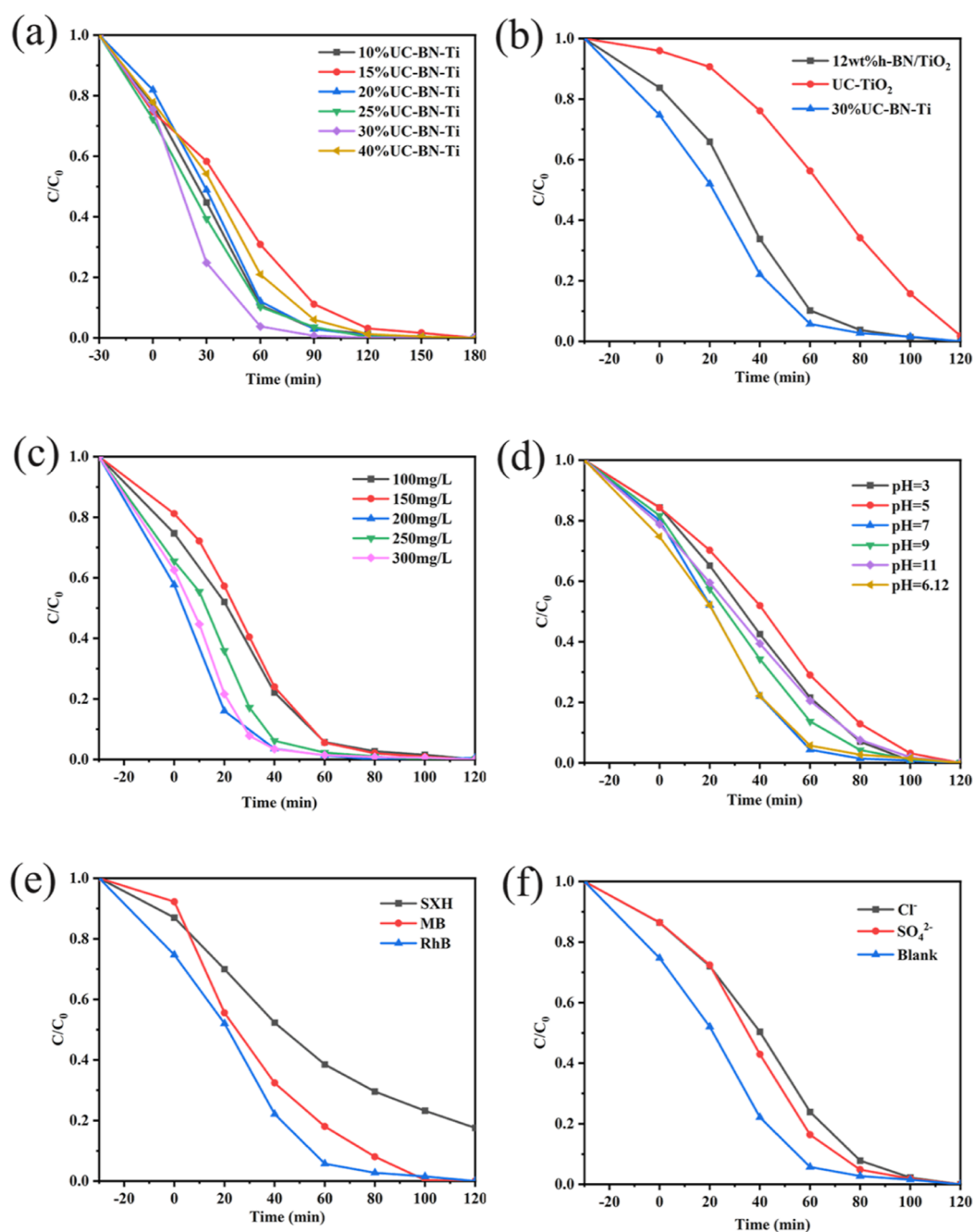
Figure 5. (a) Degradation of RhB by UC-BN-Ti at different doping ratios, (b) photocatalytic degradation of RhB by 12 wt % h-BN/TiO$_2$, UC-TiO$_2$, and 30% UC-BN-Ti, (c) degradation of RhB by 30% UC-BN-Ti at different doping quantities, (d) degradation of RhB by 30% UC-BN-Ti at different pH values, (e) photocatalytic degradation of SXH, MB, and RhB by 30% UC-BN-Ti, and (f) photocatalytic degradation of RhB by 30% UC-BN-Ti under the influence of different RhB anions.

XPS was adopted to determine the surface chemical composition and chemical state of the UC-BN-Ti sample. The XPS results are displayed in Figure 2. As shown in the survey spectrum displayed in Figure 2a, four elements (i.e., C, O, B, and Ti) were detected in UC-BN-Ti. However, the three rare-earth elements of UCNPs, namely, Y, Yb, and Tm, were not detected presumably because the entire part of the UCNPs was covered by h-BN or TiO$_2$. Figure 2b depicts the Ti 2p XPS energy spectrum of UC-BN-Ti. The peaks at 464.3 and 458.7 eV corresponded to the spin−orbit split photoelectrons Ti 2p1/2 and Ti 2p3/2, respectively, and the chemical shift of Ti 2p1/2 and Ti 2p3/2 was 5.6 eV. These results confirmed that

the valence of Ti was IV at the aforementioned time. Figure 2d depicts the O 1s XPS energy spectrum of UC-BN-Ti. The peak at 532.5 eV corresponded to the B−O−Ti bond, which indicated that TiO$_2$ and h-BN were tightly bound.[40]

TEM analysis was performed to confirm the structural properties and phase composition of the UC-BN-Ti composite. Figure 3a depicts the (101) and (002) phases of TiO$_2$ and h-BN, which have *d* values of 0.354 and 0.3 nm, respectively.[41,42] As shown in Figure 3c−k, energy-dispersive X-ray analysis confirmed the presence of different elements, such as B, N, O, Ti, Y, Yb, and Tm, in the UC-BN-Ti composite.

UV−vis diffuse reflectance spectroscopy was used to investigate the optical properties of 12 wt % h-BN/TiO$_2$, UC-TiO$_2$, and 30% UC-BN-Ti, and the results are presented in Figure 4. Figure 4a depicts the Kubelka−Munk plots of the samples, which indicate that the samples exhibited strong absorption in the UV region, as indicated by the wide absorption band between 200 and 400 nm. The band-gap widths of 12 wt % h-BN/TiO$_2$, UC-TiO$_2$, and 30% UC-BN-Ti (Figure 4b) were calculated using eq 3

$$(\alpha h \nu)^{1/2} = A(h\nu - E_g) \tag{3}$$

where α, h, ν, A, and E_g denote the absorption coefficient, Planck's constant, optical frequency, absorption intensity, and band-gap width, respectively. The documented band-gap widths of TiO$_2$ and h-BN are approximately 3.2 and 6.0 eV, respectively. However, in the present study, the band-gap widths of 12 wt % h-BN/TiO$_2$, UC-TiO$_2$, and 30% UC-BN-Ti are 3.16, 3.10, and 3.14 eV, respectively, which are marginally lower than that of TiO$_2$. This result indicated that the presence of h-BN and UCNPs improved the optical absorption capacity of TiO$_2$.[43]

Figure 4c depicts the UCL spectra of UCNPs, 30% UC-BN-Ti, and 12 wt % h-BN/TiO$_2$ under a 980 nm excitation light. The UCNPs exhibited five luminescence peaks: a purple peak at 407 nm, a blue or indigo peak at 486 nm, a red peak at 657 nm, and green peaks at 524 and 540 nm. The peak positions of 30% UC-BN-Ti were almost identical to those of the UCNPs, which indicated that 30% UC-BN-Ti contained UCNPs. The 12 wt % h-BN/TiO$_2$ sample barely emitted light, and the peak at 486 nm corresponded to double the frequency of a 980 nm laser. The UCL spectra confirmed that the ternary material contained Y$_2$O$_3$: Yb^{3+}/Tm^{3+}.

Figure 4d depicts the photocurrent response diagrams of TiO$_2$, 30% UC-BN-Ti, and 12 wt % h-BN/TiO$_2$. The photocurrent intensity of 30% UC-BN-Ti is greater than that of 12 wt % h-BN/TiO$_2$ and much greater than that of TiO$_2$. In general, the higher the current intensity, the greater the electron−hole separation ability of the material.[44] Thus, the electron−hole pair separation ability of ternary composite photocatalysts is greater than that of binary composite photocatalysts. Therefore, ternary composite photocatalysts have a higher photocatalytic activity than binary composite photocatalysts.

Nitrogen adsorption−desorption isotherms were used to determine the specific surface areas of the samples. Table S1 lists the specific surface areas, pore volumes, and pore sizes of 12 wt % h-BN/TiO$_2$ and 30% UC-BN-Ti. The specific surface area of the 30% UC-BN-Ti is 48.7 m^2 g^{-1}, which is slightly larger than the 43.4 m^2 g^{-1} of 12 wt % h-BN/TiO$_2$. As shown in Figure S1, the adsorption−desorption curves of the samples were type IV isotherms that corresponded to mesoporous structural characteristics. These isotherms contained an H1-type hysteresis loop because of the capillary coalescence of nitrogen in the mesopores of the samples, which indicated that the samples had a homogeneous pore structure. The pore size, specific surface area, and pore volume values obtained for the samples indicated that 12 wt % h-BN/TiO$_2$ and 30% UC-BN-Ti had clear mesoporous characteristics.

3.2. Photocatalytic Performance. As displayed in Figure 5a, among the prepared samples, 30%UC-BN-Ti had the strongest photocatalytic effect, and its degradation rate reached 96% after 1 h. Figure S2 depicts the kinetic curves of the

photocatalytic effects of different ratios of UC-BN-Ti. These curves were obtained by fitting the pseudo-first-order kinetic equation.[45] The 30% UC-BN-Ti sample exhibited excellent photocatalytic activity with a reaction rate constant of k = 0.0593 min^{-1}.

RhB visible-light degradation was used to investigate the photocatalytic activity of different catalysts. As shown in Figure 5b, the photocatalytic effect of 30% UC-BN-Ti was stronger than that of 12 wt % h-BN/TiO$_2$ and UC-TiO$_2$ under the same experimental conditions. This phenomenon occurred because the band-gap width and adsorption capacity of 30% UC-BN-Ti were smaller and higher, respectively, than that of h-BN/TiO$_2$. Moreover, according to the UV−vis diffuse reflection data depicted in Figure 4b, the band-gap width of UC-TiO$_2$ was smaller than that of 30% UC-BN-Ti and 12 wt % h-BN/TiO$_2$. However, the photocatalytic effect of UC-TiO$_2$ was considerably weaker than that of 30% UC-BN-Ti and 12 wt % h-BN/TiO$_2$ because of the $\pi-\pi$ adsorption of h-BN on the dye molecules and the strong separation ability of electron−hole pairs.

Figure 5c depicts the effect of the catalyst quantity on the photocatalytic behavior of UC-BN-Ti. The degradation efficiency of the RhB solution increased with an increase in the concentration of the UC-BN-Ti catalyst from 100 mg/L, regardless of the influence of adsorption in the first 30 min. However, when the concentration exceeded 200 mg/L, the photocatalytic capacity exhibited a decreasing trend, which may have been due to the increase in the turbidity of the RhB solution with an excessive quantity of the catalyst. This decrease in the photocatalytic activity caused a reduction in the light transmission rate and insufficient UV light utilization; thus, the photocatalytic efficiency decreased.

The pH value not only regulates the formation of an acid−base environment in a reaction but also strongly affects the charge distribution of a catalyst.[46] As displayed in Figure 5d, when the pH was approximately 7, the degradation effect reached its peak strength. The solution degraded faster under alkaline conditions than under acidic conditions because the point of zero charge (PZC) of TiO$_2$ is 6.8, and this phenomenon is related to the PZC of the catalyst. When the initial pH value of the solution exceeded the PZC, 30% UC-BN-Ti became negatively charged, and the positively charged RhB molecules were adsorbed on 30% UC-BN-Ti, which enhanced the degradation efficiency of RhB.

Figure 5e depicts the photocatalytic degradation of different dyes by 30% UC-BN-Ti. The RhB, MB, and SXH degradation capacities of 30% UC-BN-Ti were 94, 82, and 61%, respectively, after 1 h. In addition, the planar two-dimensional structure of the catalyst and the benzene ring in the dye molecule exhibited $\pi-\pi$ interaction, which enhanced the dye adsorption capacity. In general, azo dyes are difficult to degrade. Because SXH is an azo dye, its degradation efficiency was lower than that of RhB and MB, which are nonazo dyes.

As displayed in Figure 5f, inorganic anions inhibited the degradation of RhB by 30% UC-BN-Ti, with the inhibition effect of Cl$^-$ being stronger than that of SO$_4^{2-}$. This phenomenon was caused by the interaction between the anion and hydroxyl groups, which resulted in the deactivation of the active center of the catalyst and hindered the degradation reaction. Through adsorption on the surface of the catalyst, SO$_4^{2-}$ captured h$^+$ and OH$^-$ on its surface and converted them into other substances, which resulted in a decreased degradation efficiency. Equations 4 and 5 depict the
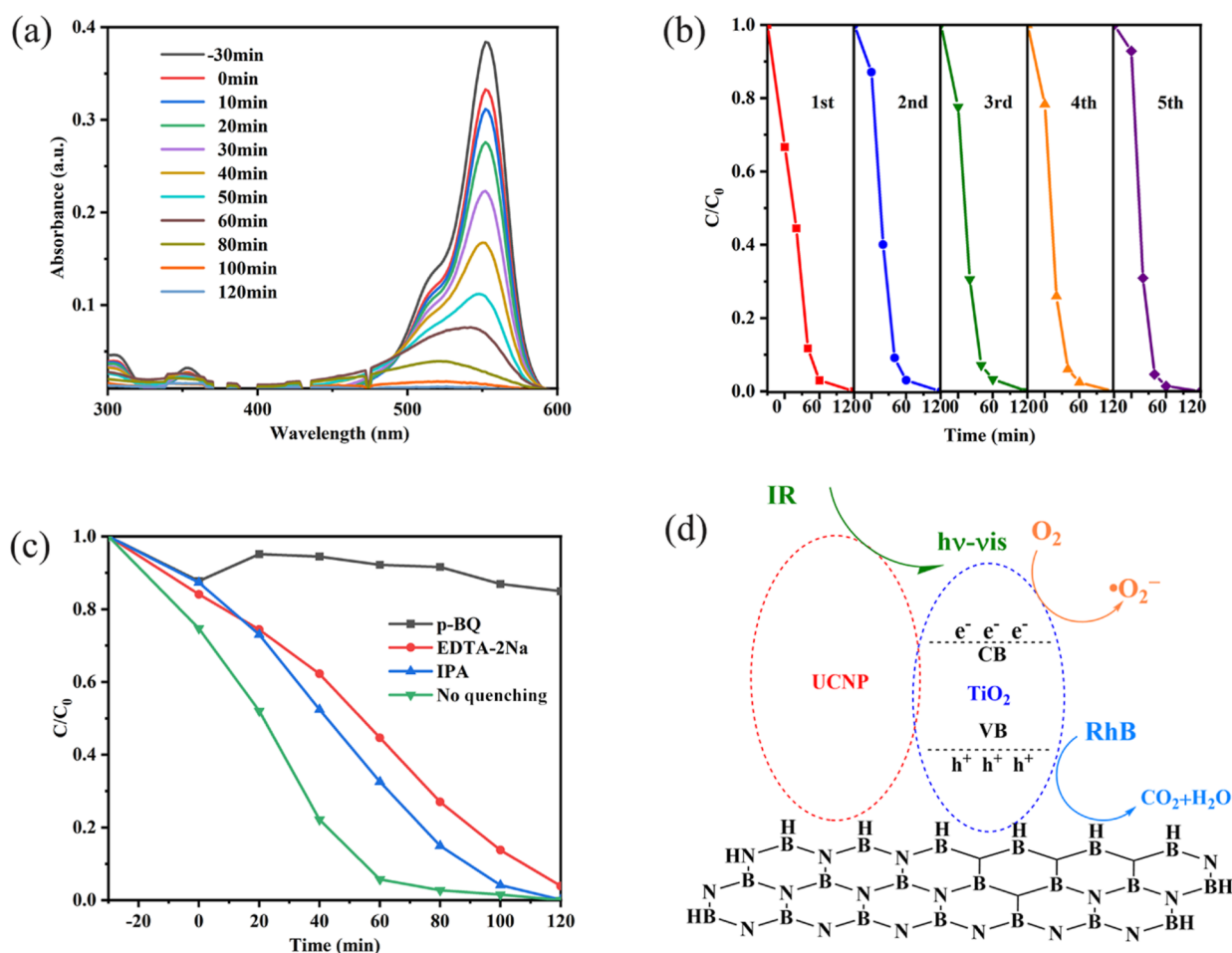
Figure 6. (a) Variation of UV−vis in 30% UC-BN-Ti photocatalytic degradation of RhB with time, (b) recycling of RhB through the photocatalytic degradation of 30% UC-BN-Ti, (c) effects of different scavengers on RhB degradation, and (d) photocatalytic mechanism of 30% UC-BN-Ti.

UV light absorption reaction of SO_4^{2-}. The degradation reaction inhibition mechanism of Cl^- was similar to that of SO_4^{2-}. In addition, Cl^- competed with the RhB molecules for the photogenerated holes and reduced the number of photogenerated holes that could react with RhB molecules, thus inhibiting the photocatalytic degradation process. Equation 6 depicts the reaction of Cl^- in the RhB solution.

$$SO_4^{2-} + h^+ \rightarrow SO_4^- \tag{4}$$

$$SO_4^{2-} + OH^\bullet \rightarrow SO_4^{\bullet-} + OH^- \tag{5}$$

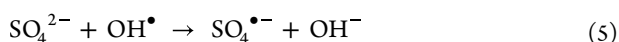$$Cl^- + h^+ \rightarrow Cl^\bullet \tag{6}$$

Figure 6a shows the UV−vis spectrum of the RhB solution catalyzed by 30% UC-BN-Ti photocatalytic with illumination time. The absorption peak of RhB dye molecules is mainly at 552 nm, and their intensity decreases with the extension of light time. Due to the absorption peak of the chromophore (azo bond) of the RhB dye molecule at 552 nm, the benzene-like ring structure and chromophore of the RhB dye molecule are destroyed during the photocatalytic reaction and gradually degraded. Examining the photochemical stability and recyclability of photocatalysts is essential to realize their practical applications. In this study, five cycling experiments were conducted to evaluate the photochemical stability and recyclability of the prepared 30% UC-BN-Ti. As shown in Figure 6b, after the five cycles, the adsorption effect of 30%
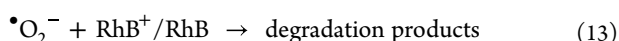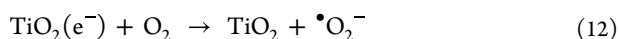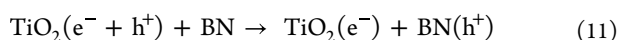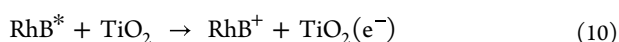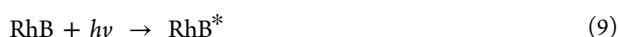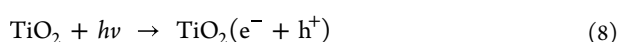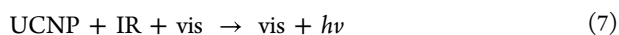
UC-BN-Ti on RhB reduced marginally, and the photocatalytic degradation effect remained unchanged. This phenomenon occurred presumably because of the blockage of the pore channel by the previously adsorbed RhB molecules with the repeated use of the catalyst, which influenced the subsequent adsorption behavior. The aforementioned results indicated that the prepared 30% UC-BN-Ti catalysts were stable, were resistant to photocorrosion, and exhibited strong photocatalytic activity when used several times.

For further exploring the mechanism of RhB degradation by 30% UC-BN-Ti, quenching experiments were conducted to confirm the active substances produced during the photocatalytic process.

During a photocatalytic reaction, numerous active free radicals with strong oxidation properties are generated, among which $^\bullet O_2^-$, $^\bullet OH$, h^+, and other active substances play a critical role in the photocatalytic degradation of organic matter. In the radical capture experiment conducted in this study, p-BQ, IPA, and EDTA-2Na were used to capture $^\bullet O_2^-$, $^\bullet OH$, and h^+. The concentration of the quenching agent is 1 mmol·L^{-1}. As shown in Figure 6c, the removal rate of RhB decreased to different extents in the presence of quenchers. The results indicated that $^\bullet O_2^-$, $^\bullet OH$, and h^+ were all involved in the photodegradation of RhB. In the presence of p-BQ, the removal rate of RhB decreased from 94 to 7.4% after 1 h of the photocatalytic reaction, which indicated that $^\bullet O_2^-$ was the most reactive species during the entire reaction. In addition,

IPA and EDTA-2Na inhibited the degradation of RhB but were less effective than *p*-BQ. Thus, the activity order of the active substances was $\bullet O_2^- > h^+ > \bullet OH$.

Our radical capture experiments confirmed the existence and participation of three radicals, namely, $\bullet O_2^-$, $\bullet OH$, and h^+, in the photocatalytic reaction. UV–vis spectral analysis indicated that RhB dye molecules were degraded in a stepwise manner during the photocatalysis process. According to Figure S3, the initial TOC content of RhB is 4.848 mg/L, and after a 2 h photocatalytic reaction, the TOC content is 2.765 mg/L. From the HPLC-MS results of Figure S4, after a 2 h photocatalytic reaction, RhB was not completely degraded into CO_2 and water. Combined with some literature analysis, some organic acids and amines were produced.[47,48] Figure 6d depicts the proposed mechanism of RhB dye wastewater degradation by 30% UC-BN-Ti. The UCNPs converted long-wavelength infrared light into short-wavelength UV and visible light. Relative to a conventional hydrogen electrode, the redox potentials of RhB and excited RhB* were 0.95 and −1.42 eV, respectively. In addition, RhB was easily oxidized in the excited state. Under light conditions, holes were left in the valence band (VB) because the electrons in the VB were excited to the conduction band (CB) as a result of the upward shift of the VB after the introduction of h-BN.[49] Simultaneously, RhB was excited (RhB*), which resulted in the injection of electrons from the adsorbed RhB* into the CB of TiO_2. Because of the introduction of h-BN with a high specific surface area, additional RhB* was concentrated on the surface of TiO_2.[50] Therefore, additional electrons were transferred to the CB of TiO_2. In addition, relative to a conventional hydrogen electrode, the reduction potential of $O_2/\bullet O_2^-$ was −0.046 eV. Therefore, the CB value of TiO_2 was sufficiently negative to reduce the adsorbed O_2 into $\bullet O_2^-$, which directly participated in the oxidation reaction. The lamellar structure and negative charge of h-BN effectively promoted the transfer of h^+ from the interior of TiO_2 to the surface, which further improved the separation of photogenerated electrons and hole pairs. As depicted in Figure S5, the VB value of TiO_2 was sufficiently positive to oxidize RhB. Thus, an h-BN sheet, as a continuous catalyst support material, played a crucial role in preventing the recombination of electrons and holes generated in a TiO_2 nanosheet. The specific reactions are outlined as follows

$$UCNP + IR + vis \rightarrow vis + h\nu \tag{7}$$

$$TiO_2 + h\nu \rightarrow TiO_2(e^- + h^+) \tag{8}$$

$$RhB + h\nu \rightarrow RhB^* \tag{9}$$

$$RhB^* + TiO_2 \rightarrow RhB^+ + TiO_2(e^-) \tag{10}$$

$$TiO_2(e^- + h^+) + BN \rightarrow TiO_2(e^-) + BN(h^+) \tag{11}$$

$$TiO_2(e^-) + O_2 \rightarrow TiO_2 + \bullet O_2^- \tag{12}$$

$$\bullet O_2^- + RhB^+/RhB \rightarrow degradation\ products \tag{13}$$

$$BN(h^+) + RhB^+/RhB \rightarrow degradation\ products \tag{14}$$

4. CONCLUSIONS

In this study, a urea precipitation method was used to synthesize flower-like UCNPs and a solvothermal method was used to synthesize a UC-BN-Ti ternary cluster photocatalyst,

which improved the photocatalytic effect of the binary h-BN/TiO_2 synthesized by other researchers. Among UC-BN-Ti composite photocatalysts, TiO_2 is the most widely used semiconductor and is characterized by high biocompatibility, physical and chemical stability, and favorable photocatalytic effects. h-BN, which is regarded as an excellent carrier material, is a stable, wide-band-gap material with a high specific surface area. The $\pi-\pi$ interaction between its two-dimensional planar structure and RhB enhances the adsorption of RhB by it. UCNPs absorb NIR light with a longer wavelength and emit UV or visible light with a short wavelength, thereby improving the light utilization capacity. According to the results of a photocurrent test conducted in this study (Figure 4d), the addition of UCNPs reduced the complexation rate of electron−hole pairs in the prepared photocatalyst. After five experimental cycles with the ternary photocatalyst, its photocatalytic behavior remained unchanged, and it remained stable. In a future study, h-BN can be further modified to improve its adsorption capacity or ability to separate electron−hole pairs for increasing the UCL efficiency of UCNPs.

■ ASSOCIATED CONTENT

Ⓢ Supporting Information

The Supporting Information is available free of charge at https://pubs.acs.org/doi/10.1021/acsomega.3c01899.

> BET surface area and pore volume of 12 wt % h-BN/TiO_2 and 30% UC-BN-Ti, nitrogen adsorption−desorption isotherms and Barret−Joyner−Halenda plots of 12 wt % h-BN/TiO_2 and 30% UC-BN-Ti, primary kinetic curves for the degradation of RhB by UC-BN-Ti, TOC image for the degradation of RhB by UC-BN-Ti, HPLC-MS images of RhB, and VB XPS spectra of 30% UC-BN-Ti samples (PDF)

■ AUTHOR INFORMATION

Corresponding Author

Yan Yuan − *School of Chemistry and Life Science, Suzhou University of Science and Technology, Suzhou, Jiangsu 215009, P. R. China;* ⓞ orcid.org/0000-0003-2831-6755; Email: yuanyanustc@163.com

Authors

Weijun Xie − *School of Chemistry and Life Science, Suzhou University of Science and Technology, Suzhou, Jiangsu 215009, P. R. China;* ⓞ orcid.org/0000-0002-5172-977X

Yue Zhang − *School of Chemistry and Life Science, Suzhou University of Science and Technology, Suzhou, Jiangsu 215009, P. R. China*

Lei Xu − *School of Chemistry and Life Science, Suzhou University of Science and Technology, Suzhou, Jiangsu 215009, P. R. China*

Dan Xie − *School of Chemistry and Life Science, Suzhou University of Science and Technology, Suzhou, Jiangsu 215009, P. R. China*

Li Jiang − *School of Chemistry and Life Science, Suzhou University of Science and Technology, Suzhou, Jiangsu 215009, P. R. China;* ⓞ orcid.org/0000-0002-5036-916X

Yanmao Dong − *School of Chemistry and Life Science, Suzhou University of Science and Technology, Suzhou, Jiangsu 215009, P. R. China*

Complete contact information is available at:
https://pubs.acs.org/10.1021/acsomega.3c01899

Notes

The authors declare no competing financial interest.

■ REFERENCES

(1) Rafiq, A.; Ikram, M.; Ali, S.; Niaz, F.; Khan, M.; Khan, Q.; Maqbool, M. Photocatalytic degradation of dyes using semiconductor photocatalysts to clean industrial water pollution. *J. Ind. Eng. Chem.* **2021**, *97*, 111−128.

(2) Rueda-Marquez, J. J.; Levchuk, I.; Fernández Ibañez, P.; Sillanpää, M. A Critical Review on Application of Photocatalysis for Toxicity Reduction of Real Wastewaters. *J. Clean. Prod.* **2020**, *258*, 120694.

(3) Maheshwari, K.; Agrawal, M.; Gupta, A. B. Dye Pollution in Water and Wastewater. *Novel Materials for Dye-containing Wastewater Treatment*; Springer: Singapore, 2021; pp 1−25.

(4) Wong, S.; Yac'cob, N. A. N.; Ngadi, N.; Hassan, O.; Inuwa, I. M. From pollutant to solution of wastewater pollution: Synthesis of activated carbon from textile sludge for dye adsorption. *Chin. J. Chem. Eng.* **2018**, *26*, 870−878.

(5) Sohni, S.; Hashim, R.; Nidaullah, H.; Lamaming, J.; Sulaiman, O. Chitosan/nano-lignin based composite as a new sorbent for enhanced removal of dye pollution from aqueous solutions. *Int. J. Biol. Macromol.* **2019**, *132*, 1304−1317.

(6) Ismail, M.; Akhtar, K.; Khan, M. I.; Kamal, T.; Khan, M. A.; M Asiri, A.; Seo, J.; Khan, S. B. Pollution, Toxicity and Carcinogenicity of Organic Dyes and their Catalytic Bio-Remediation. *Curr. Pharm. Des.* **2019**, *25*, 3645−3663.

(7) Cai, W. B.; Wang, M. Q.; Yang, G. Q.; Li, J. D. High-performance nanofiltration membranes with a polyamide-polyester composite layer and a polydopamine surface layer for desalination and dye pollutant removal. *Polymer* **2023**, *268*, 125720.

(8) Das, S.; Singh, S.; Garg, S. Agri-residual waste, wheat bran as a biosorbent for mitigation of dye pollution in industrial wastewaters. *J. Basic Microbiol.* **2022**, *62*, 465−479.

(9) Kanagaraj, J.; Senthil Velan, T.; Mandal, A. B. Biological method for decolourisation of an azo dye: clean technology to reduce pollution load in dye waste water. *Clean Technol. Environ. Policy* **2012**, *14*, 565−572.

(10) Núñez, J.; Yeber, M.; Cisternas, N.; Thibaut, R.; Medina, P.; Carrasco, C. Application of electrocoagulation for the efficient pollutants removal to reuse the treated wastewater in the dyeing process of the textile industry. *J. Hazard. Mater.* **2019**, *371*, 705−711.

(11) Salierno, G.; Napoleone, S.; Maisterrena, M. A.; Cassanello, M.; Pellasio, M.; Doumic, L.; Ayude, M. A. Continuous Heterogeneous Fenton-Type Process for Dye Pollution Abatement Intensified by Hydrodynamic Cavitation. *Ind. Eng. Chem. Res.* **2021**, *60*, 16653−16664.

(12) Qi, K. Z.; Cheng, B.; Yu, J. G.; Ho, W. A review on TiO₂-based Z-scheme photocatalysts. *Chin. J. Catal.* **2017**, *38*, 1936−1955.

(13) Du, Z.; Feng, L.; Guo, Z. L.; Yan, T. Q.; Hu, Q.; Lin, J.; Huang, Y.; Tang, C. C.; Fang, Y. Ultrathin h-BN/Bi₂MoO₆ heterojunction with synergetic effect for visible-light photocatalytic tetracycline degradation. *J. Colloid Interface Sci.* **2021**, *589*, 545−555.

(14) Song, L. L.; Jia, H. L.; Zhang, H. L.; Cao, J. L. Graphene-like h-BN/CdS 2D/3D heterostructure composite as an efficient photocatalyst for rapid removing rhodamine B and Cr(VI) in water. *Ceram. Int.* **2020**, *46*, 24674−24681.

(15) Zhu, C. S.; Zheng, J. T.; Fang, L. Y.; Hu, P.; Liu, Y. K.; Cao, X. Q.; Wu, M. B. Advanced visible-light driven photocatalyst with enhanced charge separation fabricated by facile deposition of Ag₃PO₄ nanoparticles on graphene-like h-BN nanosheets. *J. Mol. Catal. A: Chem.* **2016**, *424*, 135−144.

(16) Rafiq, U.; Wahid, M.; Majid, K. Optimized h-BN/Sb₂WO₆ Interface Mediates an Efficient Charge Separation towards Enhanced Photocatalysis. *ChemistrySelect* **2020**, *5*, 11637−11647.

(17) Wang, J. M.; Yan, H.; Long, Y. M.; Li, W. F. Enhanced photocatalytic property of a-SnWO₄ nanoplates by h-BN decorating. *J. Mater. Sci.: Mater. Electron.* **2021**, *32*, 21858−21868.

(18) Li, M. Z.; Wang, Y. O.; Tang, P.; Xie, N. H.; Zhao, Y. X.; Liu, X.; Hu, G.; Xie, J. L.; Zhao, Y. F.; Tang, J. W.; Zhang, T. R.; Ma, D. Graphene with Atomic-Level In-Plane Decoration of h-BN Domains for Efficient Photocatalysis. *Chem. Mater.* **2017**, *29*, 2769−2776.

(19) Jiang, L. B.; Yuan, X. Z.; Zeng, G. M.; Wu, Z. B.; Liang, J.; Chen, X. H.; Leng, L. J.; Wang, H.; Wang, H. Metal-free efficient photocatalyst for stable visible-light photocatalytic degradation of refractory pollutant. *Appl. Catal., B* **2018**, *221*, 715−725.

(20) Ma, Z. S.; Liu, Z.; Cheng, Z. L. A Simple and Highly Efficient Approach for Construction of 2D Nanostructured H-BN/WS₂ Heterojunction through Hydrothermal Method-Assisted Exfoliation and Their Friction Performance in Grease. *China Pet. Process. Petrochem. Technol.* **2020**, *22*, 88−93.

(21) Zhang, J.; Ma, X. L.; Song, X. M.; Hu, X. D.; Wu, E. X.; Liu, J. UV light modulated synaptic behavior of MoTe₂/BN heterostructure. *Nanotechnology* **2021**, *32*, 475207.

(22) Duan, L. J.; Wang, B.; Heck, K.; Guo, S. J.; Clark, C. A.; Arredondo, J.; Wang, M. H.; Senftle, T. P.; Westerhoff, P.; Wen, X.; Song, Y.; et al. Efficient Photocatalytic PFOA Degradation over Boron Nitride. *Environ. Sci. Technol. Lett.* **2020**, *7*, 613−619.

(23) Zhou, C. Y.; Lai, C.; Zhang, C.; Zeng, G. M.; Huang, D. L.; Cheng, M.; Hu, L.; Xiong, W. P.; Chen, M.; Wang, J. J.; Yang, Y.; Jiang, L. B. Semiconductor/boron nitride composites: Synthesis, properties, and photocatalysis applications. *Appl. Catal., B* **2018**, *238*, 6−18.

(24) Gao, X. Y.; Yao, Y.; Meng, X. C. Recent development on BN-based photocatalysis: A review. *Mater. Sci. Semicond. Process.* **2020**, *120*, 105256−105313.

(25) Fu, X. L.; Hu, Y. F.; Yang, Y. G.; Liu, W.; Chen, S. F. Ball milled h-BN: An efficient holes transfer promoter to enhance the photocatalytic performance of TiO₂. *J. Hazard. Mater.* **2013**, *244−245*, 102−110.

(26) Ansari, A. A.; Sillanpää, M. Advancement in upconversion nanoparticles based NIR-driven photocatalysts. *Renew. Sustain. Energy Rev.* **2021**, *151*, 111631.

(27) Shahid, M. Z.; Yu, L.; Mehmood, R. Tailored fabrication of triple-surface-features in well-crystalline BiOCl photocatalyst and their synergistic role in catalytic processes. *Catal. Sci. Technol.* **2020**, *10*, 2242−2253.

(28) Zhao, S. Z.; Yang, Y.; Lu, R.; Wang, Y.; Lu, Y.; Rodriguez, R. D.; Sheremet, E.; Chen, J. J. Enhanced selective adsorption and photocatalytic of Ag/Bi₂O₃ heterostructures modified up-conversion nanoparticles. *J. Environ. Chem. Eng.* **2022**, *10*, 107107.

(29) Anwer, H.; Park, J. W. Near-infrared to visible photon transition by upconverting NaYF₄: Yb³⁺, Gd³⁺, Tm³⁺@Bi₂WO₆ core@ shell composite for bisphenol A degradation in solar light. *Appl. Catal., B* **2019**, *243*, 438−447.

(30) Chang, M. Q.; Song, Y. H.; Chen, J.; Zhang, X. T.; Meng, D. Y.; Zhu, Ha.; Shi, Z.; Zou, H. F.; Sheng, Y. Multisite luminescence and photocatalytic properties of TiO₂: Sm³⁺ and TiO₂: Sm³⁺@TiO₂/ TiO₂: Sm³⁺@SiO₂ luminescent enhancement materials. *J. Alloys Compd.* **2017**, *725*, 724−738.

(31) Zhou, Y.; Wu, S. J.; Wang, F.; Li, Q.; He, C. X.; Duan, N.; Wang, Z. P. Assessing the toxicity in vitro of degradation products from deoxynivalenol photocatalytic degradation by using upconversion nanoparticles@TiO₂ composite. *Chemosphere* **2020**, *238*, 124648.

(32) Zhang, J. M.; Huang, Y.; Jin, L.; Rosei, F.; Vetrone, F.; Claverie, J. P. Efficient Upconverting Multiferroic Core@Shell Photocatalysts:

Visible-to-Near-Infrared Photon Harvesting. *ACS Appl. Mater. Interfaces* **2017**, *9*, 8142−8150.

(33) Zhao, X. Q.; Ling, Y. M.; Hao, P.; Dong, Y. Phase evolution in Bi_2O_3:Yb^{3+}/Er^{3+} nanoparticles with nearly single-band red upconversion luminescence. *Ceram. Int.* **2023**, *49*, 10829−10838.

(34) Zhao, X. Q.; Ling, Y. M.; Liu, G.; Dong, Y. The upconverted luminescence and chemical stability of morphologically controllable La_2O_3: Yb^{3+}/Er^{3+} nanoparticles. *Ceram. Int.* **2023**, *49*, 571−578.

(35) Ni, G. H.; Li, Y. H.; Wang, S. H.; Li, Q. Construction of 1D/2D BN/TiO_2 nanostructures for efficient photocatalytic degradation of dyes. *Mater. Lett.* **2021**, *288*, 129385.

(36) Li, Q.; Hou, X. M.; Fang, Z.; Yang, T.; Chen, J. H.; Cui, X. Z.; Liang, T. X.; Shi, J. L. Construction of layered h-BN/TiO_2 heterostructure and probing of the synergetic photocatalytic effect. *Sci. China Mater.* **2020**, *63*, 276−287.

(37) Wang, K.; Xue, B.; Wang, J. L.; He, Z. H.; Zhang, X. Y.; Li, S. S.; Wang, W. T.; Yang, Y.; Liu, Z. T. Efficient and selective oxidation of cyclohexane to cyclohexanone over flake hexagonal boron nitride/titanium dioxide hybrid photocatalysts. *Mol. Catal.* **2021**, *505*, 111530.

(38) Fu, X. L.; Hu, Y. F.; Zhang, T.; Chen, S. F. The role of ball milled h-BN in the enhanced photocatalytic activity: A study based on the model of ZnO. *Appl. Surf. Sci.* **2013**, *280*, 828−835.

(39) Hu, H.; Yu, L.; Gao, X. H.; Lin, Z.; Lou, X. W. Hierarchical tubular structures constructed from ultrathin TiO_2 (B) nanosheets for highly reversible lithium storage. *Energy Environ. Sci.* **2015**, *8*, 1480−1483.

(40) Chen, D. M.; Yang, D.; Wang, Q.; Jiang, Z. Y. Effects of boron doping on photocatalytic activity and microstructure of titanium dioxide nanoparticles. *Ind. Eng. Chem. Res.* **2006**, *45*, 4110−4116.

(41) Yang, C.; Wang, J. F.; Chen, Y.; Liu, D.; Huang, S. M.; Lei, W. W. One-step template-free synthesis of 3D functionalized flower-like boron nitride nanosheets for NH_3 and CO_2 adsorption. *Nanoscale* **2018**, *10*, 10979−10985.

(42) Zhang, X.; Lian, G.; Zhang, S. J.; Cui, D. L.; Wang, Q. L. Boron nitride nanocarpets: controllable synthesis and their adsorption performance to organic pollutants. *CrystEngComm* **2012**, *14*, 4670−4676.

(43) Ansari, S. A.; Khan, M. M.; Kalathil, S.; Nisar, A.; Lee, J.; Cho, M. H. Oxygen vacancy induced band gap narrowing of ZnO nanostructures by an electrochemically active biofilm. *Nanoscale* **2013**, *5*, 9238−9246.

(44) Zhou, M.; Wang, S. B.; Yang, P. J.; Huang, C. J.; Wang, X. C. Boron Carbon Nitride Semiconductors Decorated with CdS Nanoparticles for Photocatalytic Reduction of CO_2. *ACS Catal.* **2018**, *8*, 4928−4936.

(45) Xu, J.; Meng, W.; Zhang, Y.; Li, L.; Guo, C. S. Photocatalytic degradation of tetrabromobisphenol A by mesoporous BiOBr: efficacy, products and pathway. *Appl. Catal., B* **2011**, *107*, 355−362.

(46) Li, D. X.; Li, R. Q.; Zhou, D. T.; Zeng, F. J.; Yan, W. J.; Cai, S. H. The charge transfer feature and high photocatalytic activity of S-scheme TiO_2/h-BN heterostructure from first-principles. *Appl. Surf. Sci.* **2022**, *586*, 152765.

(47) Chen, J. Y.; Qin, C. C.; Mou, Y.; Cao, Y. X.; Chen, H. Y.; Yuan, X. Z.; Wang, H. Linker regulation of iron-based MOFs for highly effective Fenton-like degradation of refractory organic contaminants. *Chem. Eng. J.* **2023**, *459*, 141588.

(48) Wang, H.; Wu, Y.; Feng, M. B.; Tu, W. G.; Xiao, T.; Xiong, T.; Ang, H.; Yuan, X.; Chew, J. W. Visible-light-driven removal of tetracycline antibiotics and reclamation of hydrogen energy from natural water matrices and wastewater by polymeric carbon nitride foam. *Water Res.* **2018**, *144*, 215−225.

(49) Schneider, J.; Matsuoka, M.; Takeuchi, M.; Zhang, J.; Horiuchi, Y.; Anpo, M.; Bahnemann, D. W. Understanding TiO_2 Photocatalysis: Mechanisms and Materials. *Chem. Rev.* **2014**, *114*, 9919−9986.

(50) Wang, H.; Yuan, X. Z.; Wu, Y.; Zeng, G. M.; Chen, X. H.; Leng, L. J.; Li, H. Synthesis and applications of novel graphitic carbon nitride/metal-organic frameworks mesoporous photocatalyst for dyes removal. *Appl. Catal., B* **2015**, *174−175*, 445−454.